

Research Article

Experimental Study on Flexible Deformation of a Flapping Wing with a Rectangular Planform

Wenqing Yang ^{1,2}, Jianlin Xuan,^{1,3} and Bifeng Song^{1,3}

¹School of Aeronautics, Northwestern Polytechnical University, Xi'an 710072, China

²Research & Development Institute of Northwestern Polytechnical University in Shenzhen, Shenzhen 518057, China

³Yangtze River Delta Research Institute of Northwestern Polytechnical University, Taicang 215400, China

Correspondence should be addressed to Wenqing Yang; yangwenqing@nwpu.edu.cn

Received 5 June 2020; Revised 23 August 2020; Accepted 3 September 2020; Published 24 September 2020

Academic Editor: Seid H. Pourtakdoust

Copyright © 2020 Wenqing Yang et al. This is an open access article distributed under the Creative Commons Attribution License, which permits unrestricted use, distribution, and reproduction in any medium, provided the original work is properly cited.

A flexible flapping wing with a rectangular planform was designed to investigate the influence of flexible deformation. This planform is more convenient and easier to define and analyzed its deforming properties in the direction of spanwise and chordwise. The flapping wings were created from carbon fiber skeleton and polyester membrane with similar size to medium birds. Their flexibility of deformations was tested using a pair of high-speed cameras, and the 3D deformations were reconstructed using the digital image correlation technology. To obtain the relationship between the flexible deformation and aerodynamic forces, a force/torque sensor with 6 components was used to test the corresponding aerodynamic forces. Experimental results indicated that the flexible deformations demonstrate apparent cyclic features, in accordance with the flapping cyclic movements. The deformations in spanwise and chordwise are coupled together; a change of chordwise rib stiffness can cause more change in spanwise deformation. A certain lag in phase was observed between the deformation and the flapping movements. This was because the deformation was caused by both the aerodynamic force and the inertial force. The stiffness had a significant effect on the deformation, which in turn, affected the aerodynamic and power characteristics. In the scope of this study, the wing with medium stiffness consumed the least power. The purpose of this research is to explore some fundamental characteristics, as well as the experimental setup is described in detail, which is helpful to understand the basic aerodynamic characteristics of flapping wings. The results of this study can provide an inspiration to further understand and design flapping-wing micro air vehicles with better performance.

1. Introduction

A flapping-wing micro air vehicle (FMAV) refers to an air vehicle that can imitate flying creatures, such as birds, bats, or insects, using flapping wings to produce lift and thrust simultaneously. Flexible maneuverability can be achieved by simply adjusting the flapping parameters. An FMAV has significant advantages in mobility and also has a potentially higher efficiency compared with fixed-wing or rotary-wing air vehicles [1, 2]. Moreover, they have some additional advantages in low-altitude detection or urban combat because of their incomparable bionic performance, which has garnered considerable interest and extensive attention globally [3–5]. Owing to their small-scale and low-speed characteristics, FMAVs can be performed in a relatively

lower Reynolds number flow regime compared with regular aircrafts as the increasing air viscosity will decrease the lift-to-drag ratio of fixed wings. Natural flyers such as birds or insects have similar Reynolds number flow regime; however, they have high performance and good agility. This has inspired researchers to investigate the flight characteristics of flapping wings [6, 7].

One of the objectives of FMAV designers is to design an air vehicle that can closely mimic the abilities of natural flapping-wing flyers, such as perform agile flight at low speed, take-off or land within short ranges, turn sharply, or move acrobatically. Using high-speed cameras and stroboscopes, researchers observed that majority of the natural flyers have common deformation characteristics in their wings and can achieve higher lift and thrust by controlling their wing shape.

Furthermore, birds, bats, or insects can use their flexible wing structures to improve their aerodynamic performance and efficiency [8, 9].

The unique features of the flexible flapping wings have received significant attention from researchers. They have conducted studies through numerical simulation and experiments to evaluate the characteristics of these wings. In the case of numerical simulation of flexible flapping wings, an important aspect is to develop effective fluid-structure coupling simulation methods. Main difficulties arise owing to the small size and low mass of the flexible wing. As the flexible wings of an FMAV are commonly made of carbon fiber rods and a thin membrane structure, this type of flexible structure presents considerable difficulty in numerical simulations, particularly the simulation of the wing membrane. A typical method is to simulate the skeleton using beam elements, and the thin membrane skin using shell elements. This method can demonstrate the characteristics of idealized flexible flapping wings [10–13].

Due to the limitation of the numerical method, the experiment is a more well-conducted manner to investigate the actual flexible flapping wings to explore their unique features. Experiment is a very important and effective research method to measure the deformation parameters of the flexible flapping wings. They can be conducted to examine and validate numerical results [14], and many unique phenomena are revealed in the experimental results. However, it is not easy to conduct experiments to measure the flexible deformation with high precision. Owing to the improvement of measuring technologies, the actual deformation of a flexible flapping wing can be directly measured, and a detailed study can be conducted. This is particularly helpful for discovering any phenomenon that might have been ignored in the numerical simulation. Nan et al. [15] conducted an experimental study to investigate a flapping wing with a similar shape of a hummingbird. They found that the camber angle and aspect ratio have a critical impact on the produced aerodynamic force and efficiency. Sivasankaran et al. [16] conducted an experimental study to explore the elastic properties of a pair of dragonfly-like flapping wings. They used a high-speed imaging system to capture the flapping motions of three structurally identical wings and found that the wing with a large chordwise deformation has better performance. Deshpande and Modani [17] experimentally investigated the fluid-structure interaction characteristics of a bird-like flapping wing. They found that the trailing edge deformation pattern has a major role in thrust generation. Wu et al. [18] designed and measured a hummingbird-inspired flexible flapping wing through the experimental method. They studied several different spatial distributions of flexibility and found the frequency is crucial to thrust. Truong et al. [19] used a series of flexible wings to investigate the twisting and camber features of insect wings. They found that the wing with the uniform deformation showed a higher lift/power generation.

Since the FMAV is an integral system, each part is a component of this integral system. After some basic understandings are obtained, such as aerodynamics, aeroelasticity, and driving mechanism, the connections and influences between

each subsystem have to be considered. Karimian and Jahanbin [20, 21] developed an integrated and systematic model of an elastic two-section flapping wing based on the bond graph approach. This method can be used to investigate the effects of geometric and kinematic parameters, as well as to evaluate the controllability and sensitivity. It provided a comprehensive model that would be a suitable framework for future works in designing and optimizing the FMAV.

These literatures have provided many research results from multiple perspectives. The main concern is to imitate the shape of biological wings to carry out corresponding research. Based on these literatures, we can find that each experimental study is performed in scope to investigate a certain aspect of the characteristics of flexible flapping wings. When an FMAV designer wants to have a suitable flapping wing with an aimed performance, one needs to conduct detailed research to explore the characteristics. From the scope of wing shape, most chosen are bionic planforms, which are similar to the wings of natural flyers and also have a complex performance.

In our study, we hope to understand some more fundamental performance of flexible flapping wings with a simple rectangular planform, which is a bit different from the above-mentioned studies. Since the deformation of the flexible wing is a continuous and gradual process, we divide the flexible deformation in the spanwise and chordwise for detailed analysis. Due to the importance of flexible deformation, a detailed study was conducted through experimental methods to explore the characteristics of the designed wing. Our objective is to evaluate the different stiffness of flexible wing to determine the relationship between the deformation and aerodynamic performance. This allows a better understanding of future design and research of FMAVs. This study can extend the current research and analysis of flexible flapping wings and also provide insights into the understanding and design of FMAVs with better performance.

The remainder of this paper is organized as follows. First, we describe the design and manufacturing process of the flexible wing models. Next, we explain the use of the digital image correlation (DIC) experimental system to obtain the flexible deformation of the wing at different flapping frequencies. Subsequently, we detail the measured and collected aerodynamic characteristics. Finally, we present the analysis of the obtained data to understand the relationship between flexible deformation and aerodynamic performance.

2. Experimental Setup

2.1. DIC System. The concept of DIC was first proposed by Sutton et al. [22], who measured the deformation of a flexible structure. The system works on the principle of the space triangulation method to digital speckles on the surface of an object. The subset of the deformation position is then calculated through an intermediate handler speckle tracking mode. This method can measure the full-field displacement and strains in high precision. Lu and Cary [23] developed the second-order displacement gradient to obtain more accurate strain information. Cheng et al. [24] used the B-spline function to determine a full transformation relationship.

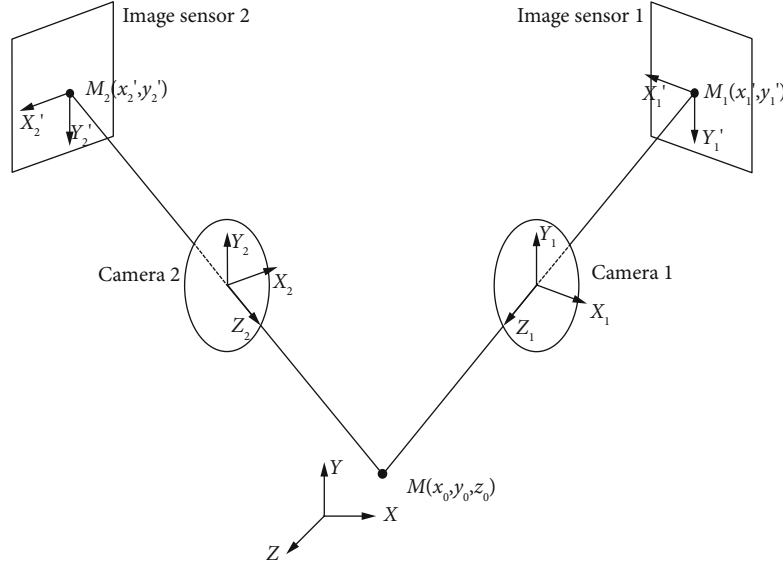


FIGURE 1: Schematic diagram of the DIC system.

The DIC system uses two cameras to achieve coordinate positioning in 3D space. Its principle is similar to that of the binocular vision. Figure 1 shows the schematic diagram of the DIC system.

The spatial point M is imaged on the image sensors using the lenses of camera 1 and camera 2. The coordinates of point M in the X - Y - Z space coordinate system are (x_0, y_0, z_0) . The coordinates of point M in the coordinate systems X_1 - Y_1 - Z_1 and X_2 - Y_2 - Z_2 of the two cameras are (x_1, y_1, z_1) and (x_2, y_2, z_2) , respectively. The coordinates of the image points of point M on the image sensors of the two cameras are (x'_1, y'_1) and (x'_2, y'_2) . Equation (1) can be obtained using the principle of optical imaging.

$$\begin{cases} (x_1, y_1, z_1) = f'_1(x'_1, y'_1), \\ (x_2, y_2, z_2) = f'_2(x'_2, y'_2). \end{cases} \quad (1)$$

This is related to the inherent parameters such as the focal length of the camera and the lens distortion coefficient. When the position of the cameras is fixed, there is a unique relationship between the coordinate system of the two cameras and the spatial coordinate system. This relationship can be expressed as Equation (2).

$$\begin{cases} (x_0, y_0, z_0) = f_1(x_1, y_1, z_1), \\ (x_0, y_0, z_0) = f_2(x_2, y_2, z_2). \end{cases} \quad (2)$$

Equation (3) is derived from Equations (1) and (2).

$$\begin{cases} (x_0, y_0, z_0) = f_1 f'_1(x'_1, y'_1), \\ (x_0, y_0, z_0) = f_2 f'_2(x'_2, y'_2). \end{cases} \quad (3)$$

Equation (3) can be further expressed as Equation (4).

$$(x_0, y_0, z_0) = f(x'_1, y'_1, x'_2, y'_2). \quad (4)$$

Equation (4) represents the relation between the spatial coordinates of the spatial point and the pixel coordinates of the point on the two cameras. This function is related to the intrinsic parameters of the two cameras and their positional relationship. In practical applications, this function is obtained through calibration. It can be seen that the system can be used to calculate the coordinate position of the point in the three-dimensional space on the basis of the position of the image point of the spatial point on the two two-dimensional images.

This DIC system has a maximum measurement speed of 480 frames/s. When the flapping frequency is 10 Hz, images in a flapping cycle have a count of 48 frames, which can almost continuously reflect the deformation process of the flexible flapping wing. The images have a resolution of 800×600 pixels, and if the space size is 50×50 cm, the displacement resolution accuracy is guaranteed to be at least 0.08 mm, which satisfies the requirements of our flexible flapping-wing deformation measurement.

The DIC system uses two cameras that capture images from different angles to achieve 3D reconstruction. Measurement requires speckles on the surface for recognition, which must not change the structural properties of the flexible wing and the aerodynamic performance. The high-speed and high-resolution cameras capture images in real time, and then, the DIC system uses its image processing software to achieve the 3D reconstruction. This enables the measurement of real-time deformation, with displacement resolution reaching 0.1%. After the camera system captures the movement of the flexible flapping wing, the absolute value of deformation can be deduced according to the position of the flapping movement-driven mechanism and the rigid



FIGURE 2: DIC system: (a) high-speed cameras and (b) light sources.

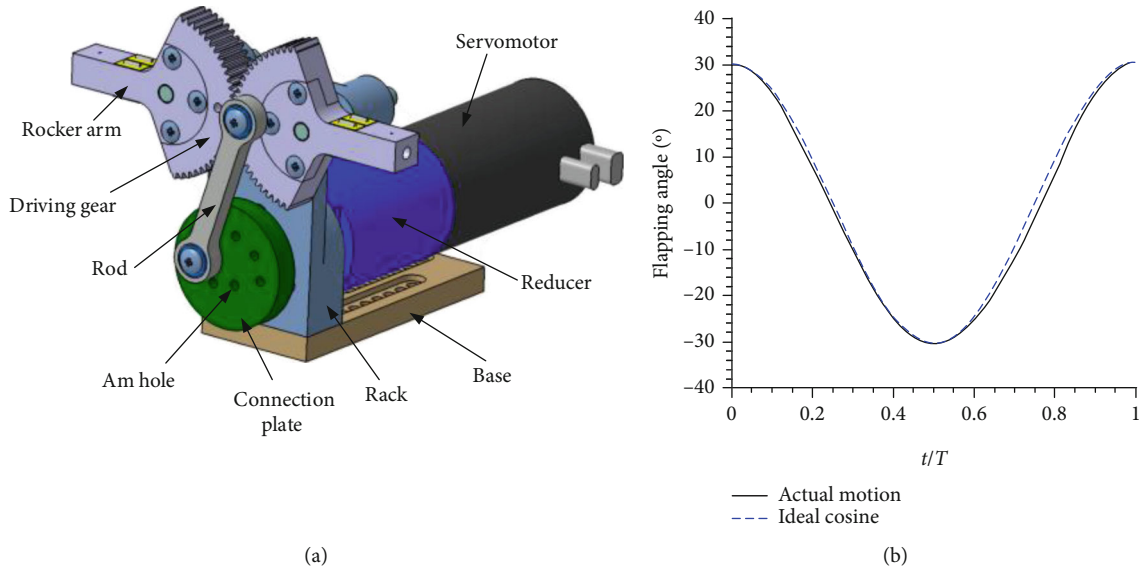


FIGURE 3: Flapping mechanism.

body displacement, which can be eliminated to calculate the absolute value of structural deformation. The experimental method can provide a more direct and objective evidence for the study of the flexible deformation [25].

The DIC system we used in this experimental research is shown in Figure 2. The focal length, direction, and distance between the two cameras are all adjustable, as shown in Figure 2(a). To ensure a suitable image definition, the camera exposure time must be as short as possible. In this case, a large amount of light source is required to ensure the brightness of the image. Two groups of powerful LED lights, two lights in each group, are used to provide sufficient light sources, see Figure 2(b).

2.2. Flapping Mechanism. The flapping mechanism adopts the four-bar linkage design to convert the rotary motion into the reciprocating swing motion of the rocker arm, as shown

in Figure 3(a). The left and right rocker arms transmit the power through the meshing between the gears, which guarantees complete symmetry of the left and right rockers. The output flapping motion of the rocker arm is a near cosine law, shown as Figure 3(b). The flapping amplitude ψ in this study is 61.0° .

The driving motor is the FAULHABER brushless servomotor, which can realize complex control functions. All the operations function under a closed-loop control, providing the equipment with a high speed and precision. The motor can return instantaneous position, speed, and current and voltage signals in real time, thereby simplifying the measuring system considerably. In addition, the motor contains the planetary gear reducer with no return differential.

2.3. Force/Torque Sensor. The sensor is one of the most important components used in an aerodynamic experiment.

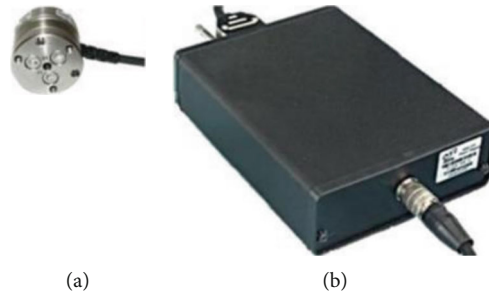


FIGURE 4: Sensor (a) and signal conditioning box (b).

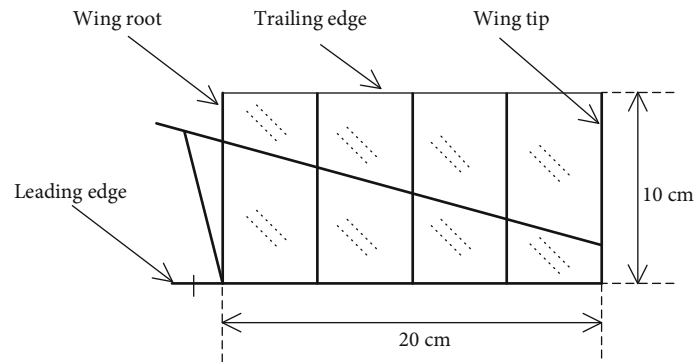


FIGURE 5: Schematic of the designed flapping-wing model.

An FMAV has a small and unsteady aerodynamic force that requires a microrange sensor with a high dynamic response. The NANO 17 sensor produced by ATI Technologies Inc., SI-12-1012, which is a force/torque sensor with six components, is used in this study. The advantages of this sensor are dynamic performance, suitable range, high sensitivity, and small volume. Figure 4 shows the sensor and signal conditioning box for the experiment.

The function of the acquisition and processing module in the experimental measurements and control software is to collect the voltage value of each channel signal, which is converted into a physical quantity and then displayed in real time.

The measured data must be stored in a disk for subsequent analysis and calculation. The complete data include the instantaneous and averaged values of each channel, as well as the parameters of the experimental environment. The experimental parameters include time, sampling rate, sampling number, flapping frequency, wind speed, air density, dynamic pressure, temperature, atmospheric pressure, angle of attack, and flapping angle.

3. Flexible Flapping-Wing Experiment

3.1. Flexible Flapping Wing. To investigate the effect of stiffness, three wings with different stiffnesses are created with the same layout. As basic exploratory research, we hope to reduce the influencing parameters as much as possible, so the planform is designed as a simple rectangle. On the one hand, the dimensions do not vary along the span- and chordwise to avoid extra curve effects. On the other hand, the rectangle can be conveniently used to define span- and chordwise

deformations, and the rate of change of deformation will not change due to the reference length. The stiffness of the flexible wing is adjusted by the diameter of the wing rib. We designed three stiffnesses.

Our research scope is concentrated in the bird size. And our experimental systems are also designed in this scale, including the test range of the sensor and the imaging range and sampling frequency of the high-speed camera system. The designed model sizes a chord length c of 10 cm and half-span length b (a single wing) of 20 cm. This size corresponds to medium-sized birds in a Reynolds number regime around 10^5 , such as pigeons and magpies. In order to make the weight of the experimental wing as small as possible, the skeleton of the wing is made of carbon fiber rods, and a thin elastic membrane is used as the skin on it. Based on the characteristics of bird wings, including the skeleton, muscle, and feather structures, their leading edge always has greater rigidity, while the trailing edge is thin feathers with high flexibility. The muscle distribution of birds' wing gradually decreases in area from the wing root to the wing tip. In order to reflect these features, the flapping wing structure we designed also has a leading edge with greater rigidity. A diagonal beam is used to reflect the feature of reduced stiffness from the wing root to the wing tip, and the trailing edge has the least stiffness with an open structure. The leading edge and oblique beams are composed of carbon rods, having diameters of 2.0 and 1.5 mm, respectively. The ribs are also made of the same material, with diameters of 0.8, 1.0, and 1.2 mm, for the 3 pairs of wings. The schematic of the designed wing model is shown in Figure 5.

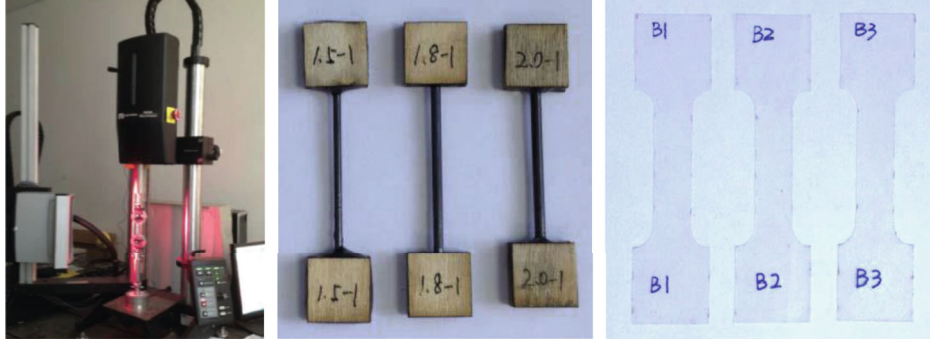


FIGURE 6: Instron 5848 machine and the testing samples.

The connection between the carbon fiber skeleton and the membrane skin is bonded by a flexible polyurethane adhesive. It guarantees substantial bond strength between them, while being elastic and not easily damaged. As the membrane is only subjected to aerodynamic forces, the skeleton is the main structural bearing element; therefore, the stiffness of the skeleton has a major influence on the structural deformation. The airfoil used in the flapping wing is a flat plate; all the rods are straight. That is, the camber effects are not considered in this study, although we try our best to avoid the influence of the airfoil camber. However, in practice, due to the manufacturing manner of the model, a certain asymmetry is still produced. In the actual model, the skin membrane is only connected to the upper surface of the carbon fiber skeleton, and the intersection of the carbon rods in the two directions is also staggered up and down and tied together, so the actual wing is not completely flat. This leads to a slight asymmetry of the generated aerodynamic force.

The material parameters are tested using the Instron 5848 machine, which is used for testing the structural properties of small samples, shown in Figure 6. The measured averaged mechanical properties of carbon fiber rods and the polyester membrane skin are shown in Table 1.

Figure 7 shows the wing marked with speckles. Each of the four ribs on the outside edge has 5 speckles, which are uniformly distributed to form a point matrix. For this point matrix, each vertical line can denote a chordwise deformation in different span sections, and each lateral line can denote a spanwise deformation in a certain chord section. The three nodes closest to the wing roots are used to determine a reference plane as displacement. A total of 23 speckles exist on each wing. The chord length c is 10 cm, and the span length of a single wing is 20 cm.

3.2. Deformation Test. The deformation test is conducted based on the binocular effect. To reconstruct a 3D image, the stereocalibration of camera parameters is necessary. To achieve this, a calibration board, with points at a fixed distance of 10 mm, is used. At least 30 clear calibration images must be captured and saved in the calibration folder to supply sufficient reference data for 3D image reconstruction.

After calibration, the image of the flapping wing is imported. The initial speckle identification is selected; when

TABLE 1: Mechanical properties of the wing.

Parameters	Value
Carbon fiber rods	
Elastic modulus	103.1 GPa
Poisson's ratio	0.34
Density	1.5 g/cm ³
Polyester membrane skin	
Elastic modulus	125.0 MPa
Density	1.4 g/cm ³

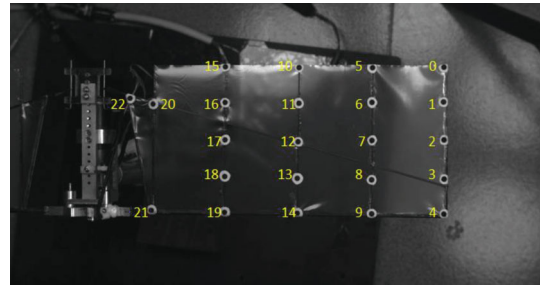


FIGURE 7: Flapping wing with speckles (same viewing angle to Figure 5).

an initial point is set in the image of camera 1 (in the case of point 0), a baseline appears in the image of camera 2. If the initial point is set in the image of camera 2, a baseline appears in the image of camera 1. If the center of the speckle in the two images is on the baseline, the calibration is correct. The calibration is completed by repeating this step for all the 23 speckles; the completed images are shown in Figure 8.

After the recognition, the speckles of the entire set of images are identified. The test system usually has the ability to automatically process data, but in fact, occasionally, there will be system errors; because of the high flapping frequency, some speckles may appear blurred and it is difficult to identify them automatically. In the data processing procedure, we need to pay more attention to every point, when an unidentified situation happened, the speckles must be correlated manually to ensure all the speckles paired to obtain their spatial coordinates. After all the speckles are identified, the 3D coordinate data of the speckle pattern can be exported.

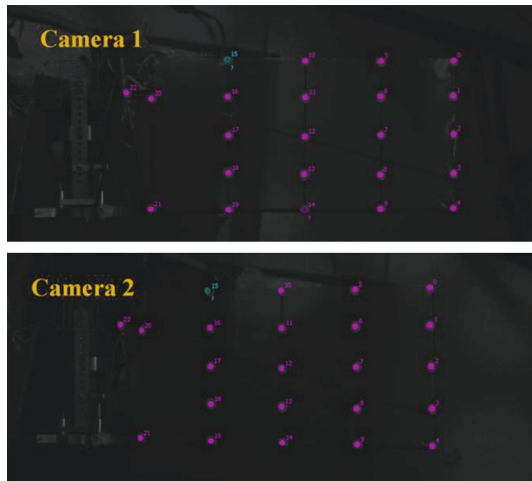


FIGURE 8: Completed speckle recognition.

3.3. Aerodynamic Test. After the dynamic deformation process measurement is completed, we need to test the aerodynamic forces. The measurement of deformation and aerodynamic force can be done simultaneously or separately. Due to the different sampling rates, the data processing of the two testes is independent, and finally, these two kinds of results can be matched through the periodic characteristics of the flapping motion. In this section, the aerodynamic test will be introduced.

The first step of the aerodynamic test is to initialize the whole test system, which is performed to clear all former data. After that, the wing is made to flap with a stable frequency. Then, we click on the record icon to save the stable data. Each test case stores data for three times. The averaged value is used to reduce experimental error. These steps are repeated to complete all the 18 sets of experimental cases with data records; the experimental cases are shown in Table 2; we tested three kinds of stiffnesses and six frequencies.

The experiments are conducted in static flow conditions, mainly focusing on the interaction between aerodynamic and structural effects, under pure flapping motion without considering the velocity of inflow. The influences of incoming flow velocity will be our future research domain.

4. Results and Analysis

The deformed surface data recorded is in the form of three-dimensional coordinates, from which the corresponding deformations can be calculated. To obtain the deformation of each speckle, the rigid body displacement has to be subtracted from the surface data. This rigid body displacement is determined from the three points, near the wing root, since we assumed that their deformation is small enough to be ignored. Thus, a plane can be defined with these three points to visualize the rigid body displacement. Finally, the deformation can be calculated as the distance of each speckle to this plane.

The rigid body surface is determined by points 20, 21, and 22, and the instantaneous distances of points 0 to 19, rel-

TABLE 2: Experimental cases.

Parameters	Value
Rib diameter (mm)	0.8, 1.0, 1.2
Flapping frequency (Hz)	3, 4, 5, 6, 7, 8

ative to the reference plane, are calculated. After data processing, the deformations of the entire flexible flapping wing are obtained.

4.1. Deformation in Spanwise and Chordwise. It is necessary to select parameters that can represent the significance of the entire flapping wing. Therefore, the deformation of the wing tip on the leading edge (point 4 relative to point 21) is used to represent the spanwise deformation. For the chordwise deformation, the outmost rib on the wing tip is chosen; the deformation of trailing edge tip minus leading edge tip (point 0 relative to point 4) is used to represent the chordwise deformation.

Since there are two directions of deformation, upward and downward, the positive direction of these deformations will be defined. First, the spanwise deformation will be illustrated. Taking the leading edge as an example, when the leading edge deformation is upward relative to its original undeformed situation, the current deformation is defined as positive, and it is negative when the leading edge deformation is downward. Similar directions are adopted for the trailing edge, positive for upward and negative for downward. Next, the direction of chordwise deformation will be defined. It is calculated as the deformation of the trailing edge minus the deformation of the leading edge. When the trailing edge has a larger deformation than the leading edge, the value of chordwise deformation is positive. Under this definition, in the downstroke, a positive chordwise deformation is thought to be beneficial to the generation of thrust similar to the wing shape of a natural flying bird. Therefore, the wing with a positive chordwise deformation during the downstroke process is likely to generate the thrust. The rigid nondeformable wing is taken as the reference plane, and its deformation is assumed to be 0.

In addition, a flapping cycle is also explained here. According to the convention, the flapping wings move from the top to the bottom, which is called the downstroke process, and then, returning from the bottom to the top is called the upstroke process. The flapping cycle is completed when a downstroke and an upstroke process is done, one after the other. In the periodic result graph shown in Figures 9, 10, 11, 12, and 13, the gray shaded area indicates the downstroke process, and the white area is the upstroke.

The deforming data of point 0 and point 4 are representative as they denote the maximum deformation of trailing edge and leading edge. The data comparison shows the speckles on the same span line and the same chord line. Regardless of the wing stiffness and flapping frequency, the speckle images show similar patterns of change. For example, in the case of the wing with a rib diameter of 1.2 mm and a flapping frequency of 8 Hz, the data regularities are shown in Figures 9 and 10. Figure 9 shows the deformations of the

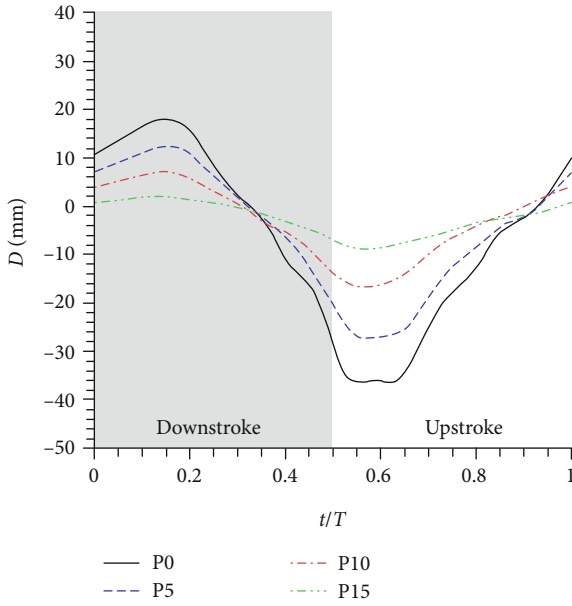


FIGURE 9: Deformation of points 0, 5, 10, and 15 on the trailing edge.

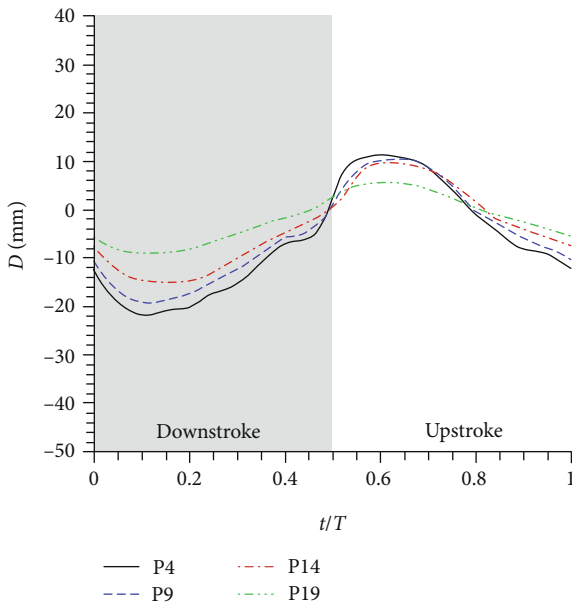


FIGURE 10: Deformation of points 4, 9, 14, and 19 on the leading edge.

points on the trailing edge in a flapping cycle, and Figure 10 depicts the deformations of the points on the leading edge in a flapping cycle. The horizontal axis is the dimensionless time in a flapping cycle. The vertical axis is the displacement of each point.

For the deformation curves of points 0, 5, 10, and 15 on the trailing edge, they are in the same span line, with the four curves having the same cycle and a similar trend, but different amplitudes. In this case, the larger the amplitude, the closer the point is to the tip. Conversely, the smaller the amplitude, the farther it is from the tip, and closer to the root.

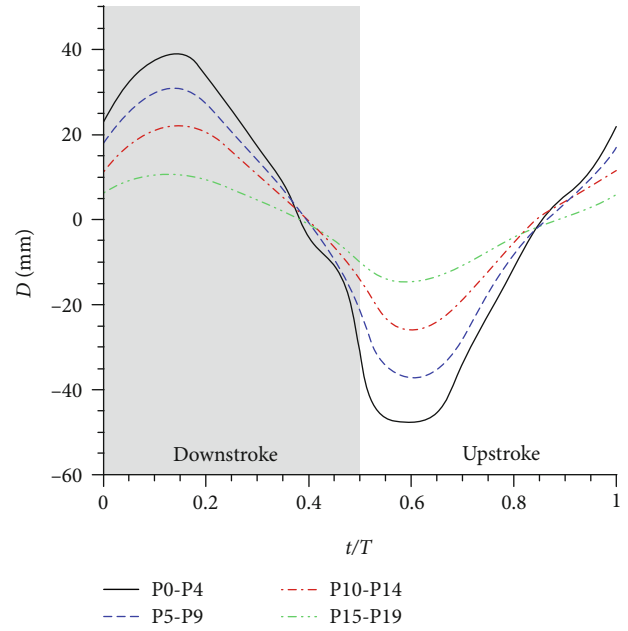


FIGURE 11: Deformation of the trailing edge compared with that of the leading edge on each rib.

The curves of points 4, 9, 14, and 19 have a similar pattern. Therefore, the span deformation can be analyzed by visualizing point 4, which is located on the leading edge and is barely affected by the chord deformation. The deformation of four points on the leading edge is shown in Figure 14.

It can be seen that for the leading edge, the deformation increases nonlinearly, along with the wingspan. It increases rapidly at the beginning, then slowly afterward. Therefore, the whole leading edge has a shape with a large root curvature and a relatively straight outer portion. This is similar to the shape of a cantilever beam after being stressed.

After the spanwise deformation has been determined, the next step is to determine the chordwise deformation. The deformations of the trailing edge compared with that of the leading edge on each rib are shown in Figure 11. The deformation on the rib of the wing tip is shown in Figure 15.

In the same flapping cycle, the curve amplitude of point 0 relative to point 4 is the largest and most representative, which shows a consistent shape with each rib. For the trailing point relative to the leading point on the four ribs, the deformations are considerably similar to each other. Therefore, the deformation of point 0, relative to point 4, can be used to represent the chordwise deformation. It can be seen that for the wing tip, the deformation increases almost linearly along the chord. For the chordwise deformation, the entire wing assumes a twisted form.

The deformation contour of the wing surface at the two near-most deformed positions ($t/T = 0.1$ and 0.6) is shown in Figure 16.

It can be seen that the deformation behavior for the wing with this type of structure shows a different trend in leading edge and trailing edge. In the two positions of maximum deformation, the deformation directions of the leading edge

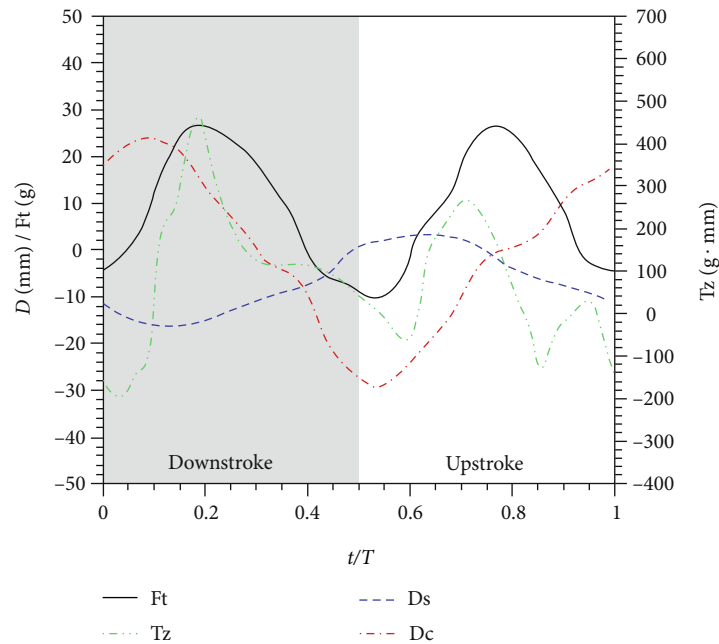


FIGURE 12: Relationship between deformation and aerodynamic characteristics in a flapping cycle.

and the trailing edge are opposite, as shown in Figures 9 and 10. The absolute value of the trailing edge deformation is greater than that of the leading edge. This kind of deformation in the opposite direction causes a high twisting moment in the wing. For the structural form of this wing, the torsion phase lags the phase of the flapping motion, in the entire flapping cycle. From an aerodynamic perspective, this form of torsion is beneficial to the aerodynamic characteristics. The reason for this deformation is due to the combined effect of aerodynamic force and inertial force. Their relationship will be analyzed in the next section.

4.2. Influences of Stiffness and Frequency. In this experiment, flapping-wing models have three different stiffnesses, and the influence of the stiffness on the deformation will be analyzed. In particular, the peak values of spanwise and chordwise deformations are selected for analysis. Figure 17 shows the spanwise and chordwise deformations of different rib diameters vary with the flapping frequency.

It can be seen that the wing with a large stiffness has a small deformation, both in the spanwise and chordwise direction. Moreover, the deformation behaviors of the three wings are similar. The flapping frequency affects the deformation. For all the three stiffness values, it is seen that increasing the flapping frequency increases both the deformations in spanwise and chordwise, significantly. Comparing the three wing stiffnesses, it can be found that they have a larger difference in spanwise deformation, as compared to that in the chordwise deformation. This phenomenon is a bit out of expectation, because all the three wings have the same leading-edge beams and oblique beams but different rib beams. The leading-edge beam and oblique beam are all alongside the spanwise, while the ribs are alongside the chordwise. The fact of different rib diameters will cause a larger difference in spanwise deformation illustrate that the

changes in local stiffness bring about changes in overall stiffness, and the stiffness of the chord structure will also cause significant changes in spanwise deformation.

As the frequency increases, the amplitude of the chordwise deformation increases, faster than the increase of the amplitude of the spanwise deformation. The increase in chordwise deformation is approximately twice of that of the spanwise deformation. A flapping wing with a higher stiffness produces a higher relative chordwise deformation, relative to spanwise deformation.

Considering the wing with a rib diameter of 1.2 mm and a flapping frequency of 6 Hz, the relationship between deformation and aerodynamic performance in a flapping cycle is shown in Figure 12. As a flat flapping wing has been considered in the absence of wind, the average lift is approximately zero, and it does not change with the change in frequency. Therefore, the impact of stiffness on the aerodynamic characteristics is discussed mainly by analyzing the thrust and generated pitching moments. Figure 12 shows the change curve of thrust and pitching moment in one flapping cycle.

It can be observed that the shape of the curves of deformation, thrust, and pitching moment is almost consistent with each other. In the given flapping cycle, the deformation curve exhibits one positive peak and one negative peak, during each half of the cycle. The thrust graph shows two peaks, which occur in the two largest deformation positions in both peaks and valleys. The pitching moment curve has a more complex shape, which shows two main peaks in each half. However, another small peak appears at the upstroke end, which might be caused by the wing asymmetry, because the wing membrane covers only the top surface of the wing skeleton. If we observe the part of the pitching moment curve at the end of the downstroke process, it can be seen that there is a small range of fluctuating values and forms a similar another peak, at the end of the upstroke. Therefore, the

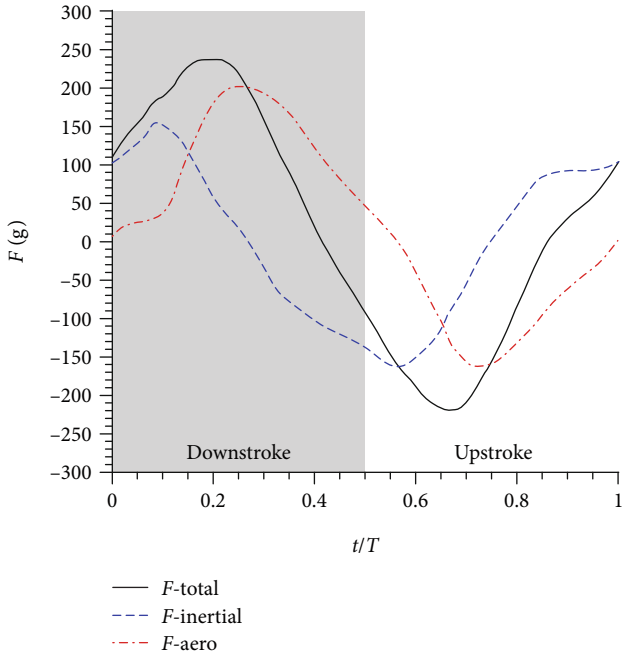


FIGURE 13: Relationship between the inertial and aerodynamic forces in a flapping cycle.

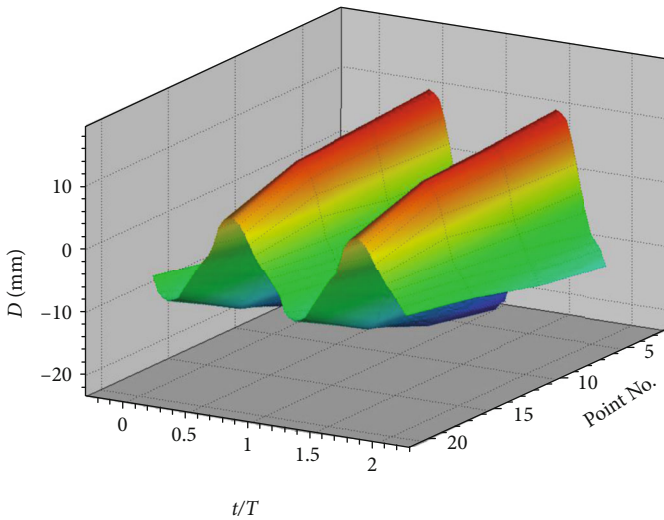


FIGURE 14: Deformation process of four points on the leading edge.

pitching moment curve shows coherence in a whole flapping cycle. The maximum values of thrust and pitching moment basically occur in the middle of the downstroke and upstroke, corresponding to the position where the flapping speed is the highest. This is also the case when the wing flaps near to its mean position.

For a flexible flapping wing, the inertial force is an important part of the wing deformation manner. We will give a brief analysis of the relationship between the flexible deformation, the aerodynamic performance, and the inertial force. Figure 13 shows the relationship between the inertial and aerodynamic forces in a flapping cycle. For a flexible struc-

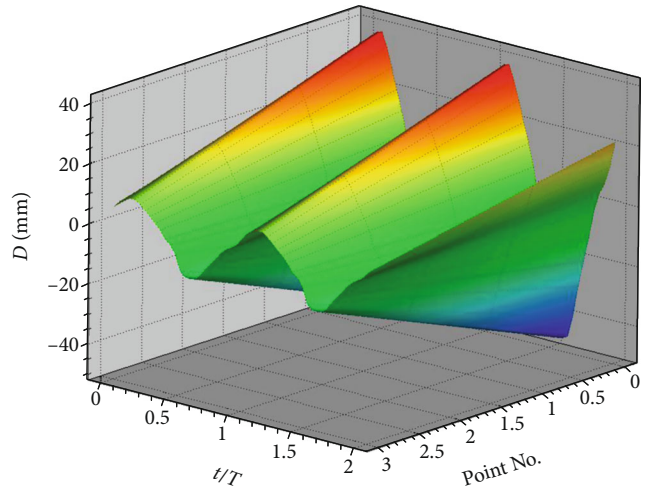


FIGURE 15: Deformation of four points on the rib of the wing tip relative to point 4.

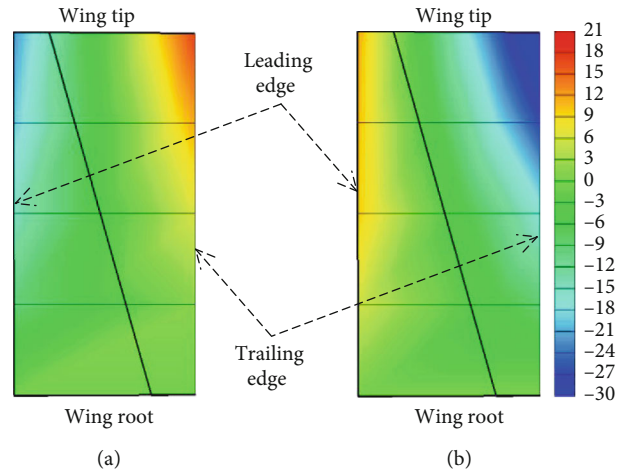


FIGURE 16: Deformation contour in a flapping cycle: (a) $t/T = 0.1$; (b) $t/T = 0.6$.

ture, the inertial force has a significant effect on the deformation and accordingly will affect aerodynamic performance. The three of them have mutual influences. In the experiments, the inertial force is hard to be measured directly, but it can be calculated through a simple formula; the mass multiplies the acceleration. In our experiment, we obtained the whole deforming process; it is easy to calculate the corresponding acceleration. After the inertial force is calculated, the pure aerodynamic force can be obtained by using the total tested force minus the inertial force.

We can see that the inertial force is at a similar scale with the aerodynamic force, so the deformation is decided together by the inertial and aerodynamic forces. The measured results are a reflection of the comprehensive effects after the final balance between the three factors. From the perspective of phase lag, the inertial force is decided by acceleration, which shows a small phase lag after the flapping movements. However, the aerodynamic force is almost proportional to the flapping velocity, which has about a quarter phase lag compare to the inertial force. Due to the combined

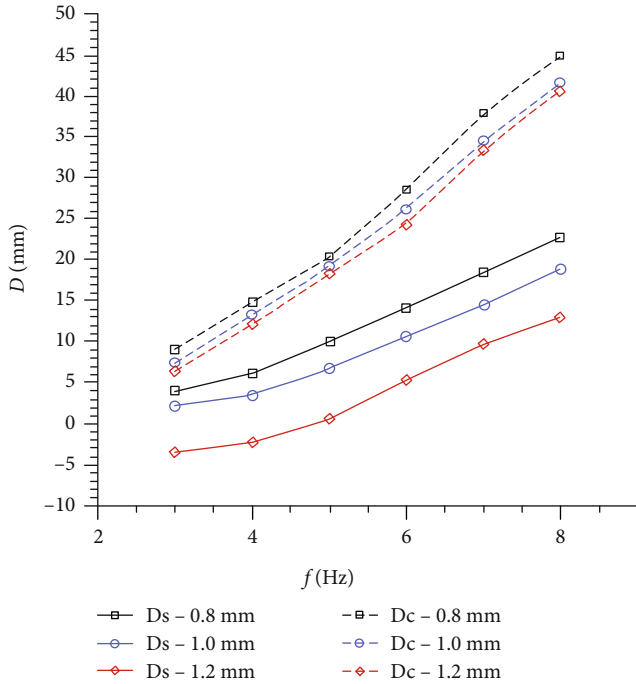


FIGURE 17: Spanwise and chordwise deformations vs. flapping frequency.

effect of the two factors, the phase of the total tested force is reflected as the combined results. The peak value of the total tested force appears between the peaks of inertial and aerodynamic forces.

In addition, the inertial and aerodynamic forces change at different rates with increasing frequency. The flapping movement is a near cosine law, which can be used to analyze their simplified relationship. Based on the law of trigonometric functions, the relationship between the inertial force and the aerodynamic force can be derived. When the flapping frequency is f , the cosine flapping movement and accordingly velocity and acceleration can be derived, see Equation (5) as follows:

$$\begin{cases} \psi(t) = A \cos(2\pi ft), \\ \psi'(t) = -2\pi f A \sin(2\pi ft), \\ \psi''(t) = -4\pi^2 f^2 A \cos(2\pi ft), \end{cases} \quad (5)$$

where A denotes the flapping amplitude and ψ is the instant flapping angle. From Equation (5), we can see the flapping velocity increases linearly with increasing frequency, while the acceleration increases squaredly with increasing frequency. Therefore, as the frequency increases, the inertial force increases more significantly than the aerodynamic force. Under the combined actions, the deformation shows an increasing speed more than linear; this phenomenon is also shown in Figure 17.

The aerodynamic force shows a positive correlation with the speed of the flapping motion, while the inertial force bears a positive correlation with the acceleration of the flapping motion. The flapping motion has a periodicity that is

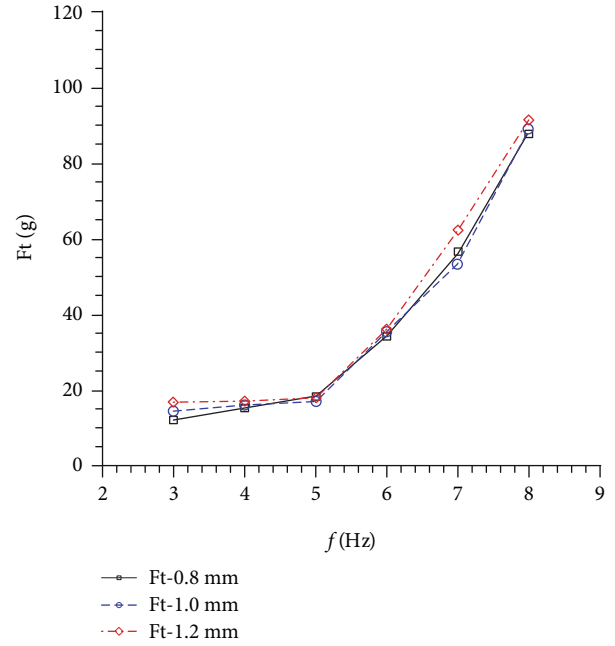


FIGURE 18: Relationship between stiffness and thrust.

often similar to that of a cosine periodic function. In this case, the phase of acceleration will lag the phase of speed by approximately a quarter of the cycle. The deformation is affected by the aerodynamic force and inertial force. In addition, the deformation will also affect the aerodynamic force and inertial force and the three will eventually reach a state of dynamic balance. The final balanced results are obtained from direct measurement through experimental methods. This allows a detailed analysis of each component.

The relationships between the stiffness and aerodynamic characteristics are shown in Figures 18 and 19. Figure 18 shows the variation of thrust force, and Figure 19 shows the variation of pitching moment.

It can be observed from Figure 18 that, in the case of the same stiffness values, the thrust increases almost exponentially, with an increase of the flapping frequency. The variation in stiffness seems to have a little effect on the thrust. Comparing Figures 18 and 17, it can be observed that the relationships of thrust and chordwise deformation are similar to each other. The chordwise deformations of the three wings are relatively close, as the corresponding thrust values. The changing rate of thrust with frequency increases more than that of the deformation with frequency. From the results, we can find the thrust is obviously affected by the frequency. The increase in frequency leads to an increase in the flapping speed, and the relationship between them is quadratic.

It can be observed from Figure 19 that when stiffness is constant, the pitching moment increases with the increase of the flapping frequency, but the trend in growth shows different increasing rates. Overall, the 1.2 mm diameter wing has the highest rate of increase of pitching moment, whereas the pitching moment of the 0.8 mm diameter wing increases relatively gently. The 1.0 mm diameter wing has an almost

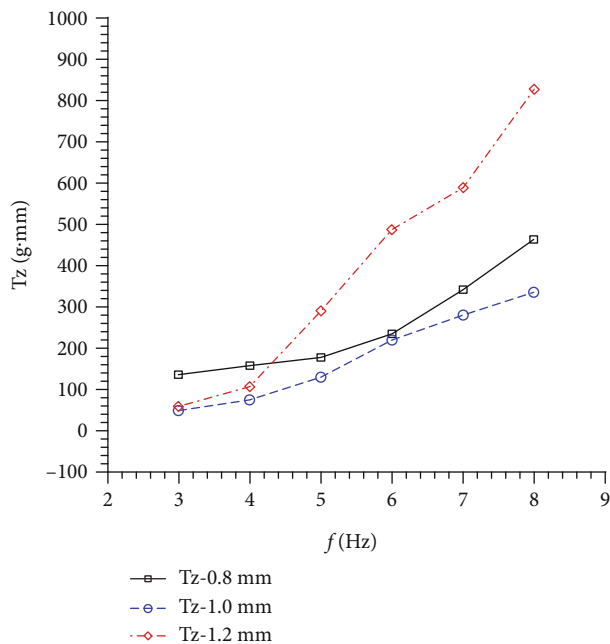


FIGURE 19: Relationship between stiffness and pitching moment.

uniform increase and has the smallest pitching moment, out of the three cases. It is seen that the stiffness has a significant effect on the pitching moment. Based on the analysis of the above results, it can be considered that both the spanwise stiffness and the mass distribution will significantly affect the pitching moment. From the results of each wing, the 1.0 mm diameter wing exhibits the best aerodynamic characteristics, in the test range. The smallest pitching moment produced indicates that the energy consumed is the smallest, and the aerodynamic efficiency is the highest.

5. Conclusions

In this study, flexible flapping wings with different stiffness values were evaluated through experiments to obtain the relationship between the flexible deformation and aerodynamic characteristics under the condition of no parallel flow. The deformation of the flapping wing was measured using a DIC system. The aerodynamic forces were obtained using the dynamic force/torque sensor with high precision and microrange.

The results indicated that the wing stiffness affects the deformation significantly. Flexible deformation exhibits stable periodic characteristics after stable flapping motion. The larger the stiffness, the smaller is the deformation. With an increase in the stiffness, the spanwise and chordwise deformations reduce almost linearly. The change in stiffness results in a larger change in spanwise deformation than in chordwise deformation.

With an increase in the frequency, the spanwise and chordwise deformations increase more than linearly. The deformation curve in spanwise and chordwise shows one peak and one valley in each flapping cycle, whereas the thrust and the pitching moment exhibit two main peaks, which occur at the deforming peak and valley. Thrust increases

exponentially with increasing frequency but shows a little change for different stiffness. According to the experimental results, the chordwise deformation has a decisive influence on the thrust.

The flexible deformation and aerodynamic and inertial forces influence each other and finally reach a state of equilibrium. The aerodynamic and inertial forces are at a similar scale of magnitude, both act together on the flexible deformation and determine its phase. As the frequency increases, the growth rate of the inertial force is greater than that of the aerodynamic force. There is a phase difference between the aerodynamic and inertial forces, which together determine the phase of the deformation, and the deformation has a feedback effect on the two, so each has a phase lag to the other factor.

When the wing stiffness is constant, an increase in the flapping frequency leads to an exponential increase in thrust. The pitching moment is the minimum when the stiffness is medium in the scope of this study. In this state, the minimum pitching moment can reduce power consumption.

From the results of this study, it is established that the deformation of the flexible wing has a significant effect on the aerodynamic characteristics, and the stiffness needs to be appropriately designed to produce a flapping wing with better overall performance.

Data Availability

The [.dat] data used to support the findings of this study are included within the supplementary information files.

Conflicts of Interest

The authors declare that there is no conflict of interest regarding the publication of this paper.

Acknowledgments

We would like to thank Editage (<http://www.editage.com/>) for English language editing. This study was supported by the National Natural Science Foundation of China (Grants 11872314 and U1613227) and the China Scholarship Council.

Supplementary Materials

Data file is in the form of columns. The first line of each column is the parameter, and the following lines show the values in order. (*Supplementary Materials*)

References

- [1] W. Shyy, H. Aono, S. K. Chimakurthi et al., "Recent progress in flapping wing aerodynamics and aeroelasticity," *Progress in Aerospace Sciences*, vol. 46, no. 7, pp. 284–327, 2010.
- [2] V. M. Mwongera, "A review of flapping wing MAV modeling," *International Journal of Aeronautics & Aerospace Research*, vol. 2, no. 2, pp. 17–26, 2015.

- [3] M. H. Dickinson, F. O. Lehmann, and S. P. Sane, "Wing rotation and the aerodynamic basis of insect flight," *Science*, vol. 284, no. 5422, pp. 1954–1960, 1999.
- [4] G. V. Lauder, "Flight of the robofly," *Nature*, vol. 37, no. 4, pp. 341–347, 2001.
- [5] J. R. Usherwood and C. P. Ellington, "The aerodynamics of revolving wings I. Model hawkmoth wings," *Journal of Experimental Biology*, vol. 205, no. 11, pp. 1547–1564, 2002.
- [6] R. B. Srygley and A. L. R. Thomas, "Unconventional lift-generating mechanisms in free-flying butterflies," *Nature*, vol. 420, no. 6916, pp. 660–664, 2003.
- [7] H. Wang, L. Zeng, H. Liu, and C. Yin, "Measuring wing kinematics, flight trajectory and body attitude during forward flight and turning maneuvers in dragonflies," *Journal of Experimental Biology*, vol. 206, no. 4, pp. 745–757, 2003.
- [8] D. Colmenares, R. Kania, W. Zhang, and M. Sitti, "Bio-inspired flexible twisting wings increase lift and efficiency of a flapping wing micro air vehicle," 2020, <https://arxiv.org/abs/2001.11586>.
- [9] S. A. Combes, "Flexural stiffness in insect wings I. Scaling and the influence of wing venation," *The Journal of Experimental Biology*, vol. 203, pp. 2979–2987, 2006.
- [10] Z. Jianyang, J. Lin, and H. Yu, "Aerodynamic performance of the three-dimensional lumped flexibility bionic hovering wing," *International Journal of Aerospace Engineering*, vol. 2018, Article ID 1314258, 14 pages, 2018.
- [11] T. Nakata, H. Liu, Y. Tanaka, X. Wang, and A. Sato, "Aerodynamics of a bio-inspired flexible flapping-wing micro air vehicle," *Bioinspiration & Biomimetics*, vol. 6, no. 4, article 045002, 2011.
- [12] N. Lee, S. Lee, H. Cho, and S. Shin, "Effect of flexibility on flapping wing characteristics in hover and forward flight," *Computers & Fluids*, vol. 173, pp. 111–117, 2018.
- [13] G. A. Tzezana and K. S. Breuer, "Thrust, drag and wake structure in flapping compliant membrane wings," *Journal of Fluid Mechanics*, vol. 862, pp. 871–888, 2019.
- [14] J. Lankford, *Experimental and coupled CFD/CSD investigation of flexible MAV-scale flapping wings in hover*, Dissertation, University of Maryland, College Park, 2018.
- [15] Y. Nan, M. Karásek, M. E. Lalami, and A. Preumont, "Experimental optimization of wing shape for a hummingbird-like flapping wing micro air vehicle," *Bioinspiration & Biomimetics*, vol. 12, no. 2, article 026010, 2017.
- [16] P. N. Sivasankaran, T. A. Ward, E. Salami, R. Viyapuri, C. J. Fearday, and M. R. Johan, "An experimental study of elastic properties of dragonfly-like flapping wings for use in biomimetic micro air vehicles (BMAVs)," *Chinese Journal of Aeronautics*, vol. 30, no. 2, pp. 726–737, 2017.
- [17] P. Deshpande and A. Modani, "Experimental investigation of fluid–structure interaction in a bird-like flapping wing," *Journal of Fluids and Structures*, vol. 91, p. 102712, 2019.
- [18] P. Wu, B. K. Stanford, E. Sällström, L. Ukeiley, and P. G. Ifju, "Structural dynamics and aerodynamics measurements of biologically inspired flexible flapping wings," *Bioinspiration & Biomimetics*, vol. 6, no. 1, article 016009, 2011.
- [19] T. V. Truong, Q. V. Nguyen, and H. P. Lee, "Bio-inspired flexible flapping wings with elastic deformation," *Aerospace*, vol. 4, no. 3, p. 37, 2017.
- [20] S. Karimian and Z. Jahanbin, "Bond graph modeling of a typical flapping wing micro-air-vehicle with the elastic articulated wings," *Meccanica*, vol. 2020, pp. 1–32, 2020.
- [21] S. Karimian and Z. Jahanbin, "Aerodynamic modeling of a flexible flapping-wing micro-air vehicle in the bond graph environment with the aim of assessing the lateral control power," *Proceedings of the Institution of Mechanical Engineers, Part G: Journal of Aerospace Engineering*, vol. 233, no. 13, pp. 4998–5015, 2019.
- [22] M. Sutton, W. Wolters, W. Peters, W. Ranson, and S. McNeill, "Determination of displacements using an improved digital correlation method," *Image and Vision Computing*, vol. 1, no. 3, pp. 133–139, 1983.
- [23] H. Lu and P. Cary, "Deformation measurements by digital image correlation: implementation of a second-order displacement gradient," *Experimental Mechanics*, vol. 40, no. 4, pp. 393–400, 2000.
- [24] P. Cheng, M. Sutton, H. Schreier, and S. McNeill, "Full-field speckle pattern image correlation with B-spline deformation function," *Experimental Mechanics*, vol. 42, no. 3, pp. 344–352, 2002.
- [25] C. Tay, C. Quan, Y. Huang, and Y. Fu, "Digital image correlation for whole field out-of-plane displacement measurement using a single camera," *Optics Communications*, vol. 251, no. 1–3, pp. 23–36, 2005.